Carbon Trends 21 (2025) 100589

Contents lists available at ScienceDirect

Carbon Trends

journal homepage: www.elsevier.com/locate/cartre

Robust reflection asymmetry across rhombohedral—Bernal stacking boundaries in trilayer graphene

Géza I. Márk [a,*,1], Márton Szendrő [a,1], Alexandre Mayer [b,c], Zoltán Simon [d], Péter Vancsó [a]

[a] HUN-REN Centre for Energy Research, Institute for Technical Physics and Materials Science, Budapest, Hungary
[b] Department of Physics, University of Namur, Belgium
[c] Namur Institute for Complex Systems (naXys), University of Namur, Belgium
[d] Department of Control Engineering and Information Technology, Budapest University of Technology and Economics, Budapest, Hungary

ARTICLE INFO

Keywords:
Graphene
Graphite
Trilayer graphene
Rhombohedral graphene
Wave packet dynamics
Pseudopotential
Band structure
DFT
Effective mass
Pseudospin
Layer polarization
Inversion symmetry

ABSTRACT

We report a pronounced direction-dependent quantum transport phenomenon across stacking domain boundaries in trilayer graphene, revealed by large-scale wave packet dynamics simulations. Employing molecular statics with realistic interatomic force fields, we construct an ABC–ABA grain boundary geometry with structural features – such as soliton width and corrugation amplitude – that closely match experimental observations. To mimic a transport device geometry, we injected electrons from a graphene electrode into the outer layer of our ABC-ABA junction. We demonstrate that this configuration shows a striking asymmetry in transport behavior: wave packets incident from the rhombohedral (ABC) side transmit with minimal reflection, while those originating from the Bernal (ABA) side are strongly backscattered. The total reflection probability measured in the graphene electrode differs by more than a factor of 20 between the two incidence directions, and the energy-dependent transmission function reveals that the main differences are concentrated within the ±0.5 eV energy range around the Fermi level. We prove that this rectification is robust across grain boundaries of varying thicknesses and morphologies, as it originates from the distinct electronic structures – effective masses, sublattice-, and layer polarizations – of the two stacking configurations. These differences in the electronic structure of the two stacking configurations are rooted in their lattice symmetries: the mirror-symmetric ABA and the inversion-symmetric ABC trilayers, which give rise to distinct reflection behavior at both the graphene-trilayer contact and the ABA–ABC grain boundary. The precise energy dependence of the reflection function, however, depends on the specific atomic structure of the domain boundary, yet, without altering the overall value of the reflection. Our results show that contacted ABC–ABA stacking domain boundaries could lead to directional quantum transport — opening a pathway toward quantum diode-like functionalities.

1. Introduction

Grain boundaries (GBs) represent ubiquitous structural defects in polycrystalline two-dimensional (2D) materials, profoundly influencing their macroscopic properties [1,2]. These interfaces significantly impede or modify the coherent transmission of electrons due to localized strain fields and altered bonding configurations acting as scattering centers or potential barriers within the materials electronic landscape [3]. These combined effects contribute to a complex interplay that dictates the overall conductance and can even lead to anisotropic or rectified electron flow [4]. Consequently, understanding electron transport across such boundaries is critical for both fundamental condensed matter physics and for the development of high-performance 2D material-based electronic devices. In graphene, specifically, the presence of grain boundaries can drastically alter its exceptional electronic characteristics [5–9], moving beyond the ideal ballistic transport often envisioned [10]. In multilayer systems, grain boundaries exhibit even greater complexity, arising from stacking misalignments that can occur also vertically due to relative translations between the layers [11,12].

Rhombohedral (ABC-stacked) graphene is a less common, but increasingly studied allotrope of multilayer graphene that exhibits distinct electronic properties compared to the more prevalent Bernal (ABA or AB-stacked) form [13]. The rhombohedral stacking features

* Corresponding author.
E-mail address: mark.geza@ek.hun-ren.hu (G.I. Márk).
[1] These authors contributed equally to this work.

https://doi.org/10.1016/j.cartre.2025.100589
Received 18 June 2025; Received in revised form 25 October 2025; Accepted 1 November 2025
Available online 10 November 2025

a staggered intra- and interlayer hopping pattern [14], similar to a one-dimensional (1D) Su–Schrieffer–Heeger (SSH) model [15], which results in a flat electronic band and an increased charge density on the surface at the Fermi-level [13]. Recent transport [16–18] and Scanning Tunneling Microscopy (STM) measurements [19–21] in few layers ($n = 3, 4, 5$) thick samples revealed strong correlation effects in the flat band, such as fractional quantum anomalous Hall states and superconductivity at low temperatures. In contrast, AB-stacked multilayers do not exhibit such flat bands but instead display parabolic low-energy dispersion, which lacks the high density of states.

Since natural graphite contains ABC stacking in about 5%–15% [22] of cases, it is not surprising that ABC–ABA transitions are not uncommon in exfoliated samples. The simplest interface between rhombohedral (ABC) and Bernal (ABA) stacked graphene necessitates a minimum of three layers to accommodate both stacking orders contiguously. Experimental studies using Raman mapping (2D-mode) [23,24], near-field infrared nanoscopy [25,26] and conductive atomic force microscopy (c-AFM) [27] have confirmed the existence of ABC-ABA interfaces in trilayer samples and even show the possibility to control their motion. However, these methods are unable to reveal the exact atomic configuration of these grain boundaries, thus a detailed theoretical study is necessary to elucidate their structural properties.

The experimentally observed trilayer ABC-ABA junctions highlight the importance of investigating the fundamental electronic transport phenomena that occur at such interfaces. The transport properties of interfaces between ABC and ABA stacked trilayer graphene depend on a combination of factors.

First, the distinct electronic band structures of the ABC and ABA regions on either side of the interface dictate the behavior of electrons approaching and traversing the junction. At low energies ($|E| < 0.5$ eV), ABA trilayer graphene hosts two types of low-energy bands – a linear band resembling that of monolayer graphene and a parabolic band characteristic of Bernal bilayer graphene – whereas ABC trilayer graphene features a single band with cubic dispersion that remains nearly flat near the Fermi level. The sublattice symmetry and layer polarization is also different for the two stacking configurations. This distinction is driven by their inherent lattice symmetries: ABA stacking possesses mirror symmetry with respect to its middle layer but lacks an inversion center, whereas ABC stacking exhibits inversion symmetry about the middle layer but no horizontal mirror plane.

Second, the atomic-scale structure and electronic states within the interface region itself play a role, acting as a unique scattering or transmission medium that modifies electron flow relative to the bulk properties of either stacking domain.

In addition, in a transport geometry, we also have to take into account the role of the contacts through which the electrons are injected into the geometry [28,29]. Therefore, understanding both the bulk electronic properties and the interface-specific characteristics together with the electrodes is essential for predicting and controlling charge transport at these stacking domain boundaries.

Some of these effects have previously been investigated in the literature. Focusing solely on the effect of the distinct band structures of ABC and ABA trilayers Mouhafid et al. [30] demonstrate that the transmission probability and conductance of a simple connected ABC–ABA–ABC trilayer graphene junction exhibit Klein tunneling, along with its modulation by potential barriers and interlayer bias. In order to consider the effect of the junction geometry Grandadam et al. [31] modeled a simplified interface to represent the stacking fault between trilayer ABC and ABA regions by using local compression or shear of atomic bonds. In that tight-binding study the authors found that interface bands form in these regions, particularly pronounced for armchair-type interfaces, and these bands become quantized into discrete energy levels in finite-size structures.

While these simplified models with narrow (few unit cells wide) grain boundaries provide valuable initial insights, more realistic geometry models are essential for capturing the full complexity of the grain boundaries. In contrast to these simplified models the experimental ABC-ABA grain boundaries can extend over 20 nm as measured by STM [32]. This large spatial extent of the GB presents a substantial challenge for accurate Density Functional Theory (DFT) calculations, particularly in terms of reliable geometry prediction. Therefore, constructing such realistic geometric models requires the use of molecular dynamics simulations to relax the atomic structure at the interface, naturally capturing bond distortions and local reconstructions [33].

Calculating the transport properties of realistic ABC-ABA grain boundaries with electrodes is similarly affected by size limitations, since DFT simulations that capture the electronic structure and quantum transport in these systems become computationally infeasible. Thus, alternative approaches are necessary to predict the electronic and transport properties of these grain boundaries. Wave packet dynamics (WPD) [34] offers a powerful and efficient solution, because it allows us to simulate the time evolution of electrons as they propagate through the complex potential landscapes. This method has several advantages: it can handle large systems, it naturally incorporates quantum interference effects, and it provides a real-space picture of electron propagation, offering insights into scattering and transmission mechanisms that are difficult to obtain from traditional band structure methods. By using the split-operator technique, the WPD method was successfully applied previously in graphene-based structures, where the system was described by continuum Hamiltonians [35,36] or tight-binding Hamiltonians [37–39]. Although these Hamiltonians facilitate rapid calculations, they do not easily incorporate defects in the system, such as stacking fault defects. Even in the case of the tight-binding Hamiltonian, where the atoms are handled explicitly, careful investigation and a fitting procedure based on density functional theory (DFT) calculations are required to parametrize the different defects in the TB model. To overcome this difficulty, we used our recently developed pseudopotential [40] to construct the Hamiltonian, which correctly describes the electronic structure of multilayer graphitic systems. The unique advantage of this pseudopotential method is that it can handle stacking fault defects and even atomic scale defects as we demonstrated earlier when modeling realistic single-layer graphene GB environments [41,42]. While the tight-binding Hamiltonian handles the atomic sites, the pseudopotential calculation is based on a real-space grid during the split-operator FFT calculations. Therefore, it is computationally more expensive, however it provides a reliable framework for the ABC-ABA GB transport analyses presented herein.

This paper is organized as follows: In Section 2, we detail the construction of the realistic GB geometry using molecular statics simulations. Section 3 then presents the WPD transport calculations performed within a realistic GB transport device geometry. This section elucidates the electron transmission characteristics and provides a detailed, microscopic explanation of the scattering processes. Finally, Section 4 provides the conclusions drawn from our study.

2. Molecular statics relaxation of the grain-boundary

Previous theoretical models [24,31,43,44] often used simulation cells much smaller than experimental scales, resulting in unrealistically narrow domain walls and excessive strain. Many also neglected atomic relaxation [31] or produced only minimal corrugations [24], inconsistent with experimental observations [32]. While a recent large-scale model by Dey et al. [33] used mechanical pulling, it introduced edge disorder that breaks structural symmetries crucial for transport studies. Here, we construct large, symmetry-preserving grain boundaries by encoding the stacking transition explicitly into the initial geometry. Subsequently, this initial geometry is relaxed, yielding controlled solitonic boundaries that preserve the key symmetries of the system while spanning length scales comparable to experimental observations.

In this study (see Fig. 1), a solitonic stacking domain boundary between ABC (rhombohedral) and ABA (Bernal) trilayer graphene was constructed and analyzed using classical molecular statics simulations.

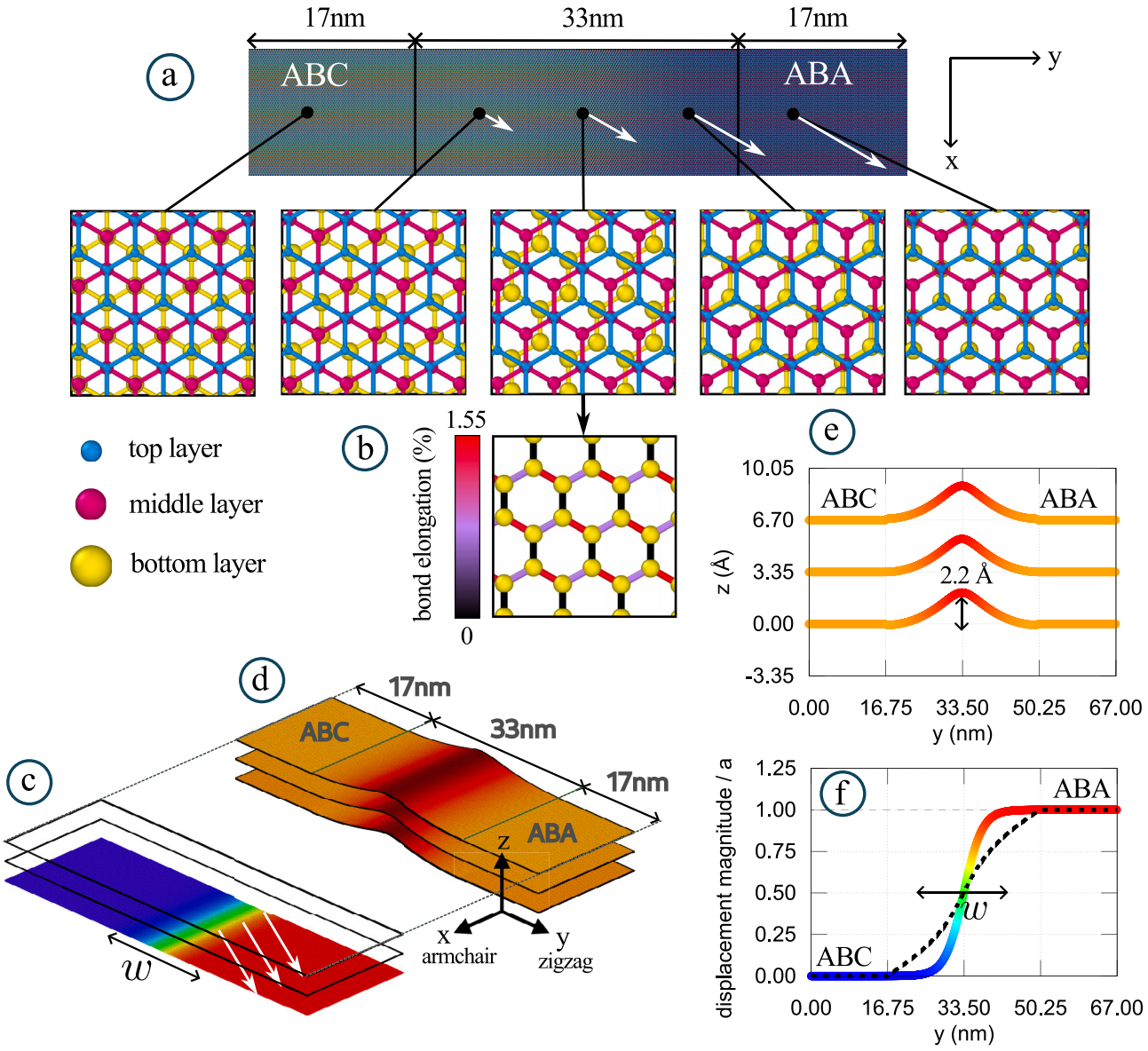

Fig. 1. Construction and relaxation of the ABC–ABA domain structure used in molecular statics simulations. (a) Top view of the initial flat trilayer graphene ribbon with an in-plane displacement field applied to the bottom layer (yellow), inducing a transition from ABC to ABA. Insets show the gradual shift of the bottom layer across the boundary. For each inset, white arrows indicate the displacement vectors, exaggerated for visual purposes. The spheres representing the atomic positions are drawn progressively thicker in each layer (layer 1: small cyan, layer 2: medium size magenta, layer 3: large yellow), in order to visualize the stacking of the layers. (b) Bond elongation map in the bottom layer at the boundary center (middle inset in (a)), with a maximum strain of 1.55% along the armchair direction. (c) Perspective view of the initial flat geometry showing the displacement field magnitude in the bottom layer (color-coded). White arrows indicate the armchair displacement direction, oblique to the grain boundary (green). $w = 20$ nm denotes the soliton width. (d) Relaxed geometry after LAMMPS minimization, showing out-of-plane wrinkles at the domain boundaries. (e) Side view of the relaxed structure, showing vertical corrugation profiles using the same color coding values as in (d). (f) In-plane displacement profile before (colored) and after (black) relaxation, indicating a smoother transition across the boundary. The color coding represents the same values of displacement as in (c).

As shown in Figs. 1a and 1c, the model system was initialized with a flat, fully ABC-stacked trilayer graphene ribbon with a total length of 67 nm and a width of 0.426 nm (3 carbon–carbon bond lengths). The ribbon was oriented such that its longitudinal axis (y-axis) aligned with the zigzag direction, while its transverse axis (x-axis) corresponded to the armchair direction. Periodic boundary conditions were applied exclusively along the x-axis. To induce a transition between stacking orders, a position-dependent displacement field was applied to the bottom layer along an in-plane armchair direction (see white arrows in Fig. 1a and c). This choice is motivated by the fact that, when shifting a layer along a straight path, transitions between distinct high-symmetry stacking configurations – such as ABC, ABA, or AAB – are only possible along the armchair direction, with the shift magnitude corresponding to an integer multiple of the carbon–carbon bond length. We defined the displacement profile along these directions to follow a sigmoid-type smoothed steplike function centered at y_0 (the middle of the domain wall) to interpolate between the unshifted and shifted regions of the layer (see Fig. 1f):

$$\Delta D_i(y, y_0) = \frac{\delta_i}{2}\left(\tanh\left(\frac{y - y_0}{\Lambda}\right) + 1\right) \quad (1)$$

where i denotes the layer index, Λ parameter is proportional to the characteristic width (w) of the domain wall, and the magnitude of the deformation is

$$\delta_i = n_i a, \tag{2}$$

with a being the carbon–carbon bond length and n_i is an integer, specifying the displacement in layer i. By assigning the relative displacements in each layer, the vector $\vec{n} = [n_1, n_2, n_3]$ serves as a key descriptor of the type of the stacking transitions, encoding the total strain applied in the GB. The formula in Eq. (1) ensures a continuous transition in stacking order while localizing the strain over a finite domain wall width (w), where Λ was chosen so that $w \approx 20$ nm, thereby setting an experimentally motivated value. Figs. 1c and 1f provide a visual representation of the shift profile of Eq. (1). Since the displacement direction (white arrows in Fig. 1a and c) is not orthogonal to the stacking domain boundaries (green areas in Fig. 1c), the resulting solitons exhibit both shear and tensile character—yielding a mixed-type domain wall configuration. The nature of a stacking domain boundary – whether tensile, shear, or mixed – is determined by the direction of atomic displacement relative to the boundary normal [25,45]. A purely tensile soliton arises when the interlayer shift is oriented perpendicular to the domain wall, leading to uniform compression or extension across the boundary. Conversely, a pure shear soliton forms when the displacement is parallel to the domain wall, resulting in relative sliding between layers without significant normal strain. In the present case, the displacement direction is oblique with respect to the boundary orientation, producing a soliton that involves both relative sliding and dilation components. This gives rise to a mixed-type stacking domain wall, exhibiting both shear and tensile strain characteristics. Such non-pure shear transitions are commonly observed in experimental systems, particularly in multilayer graphene samples where strain fields and substrate interactions lead to complex interlayer displacements [25,46–50].

There are infinite possible sets of $n_i = 1, 2, 3, 4 \ldots$ values that can achieve the rhombohedral-hexagonal transition, however, most of them are unphysical due to the enormous strain that they encode. In selecting suitable $\vec{n}$ vectors, we prioritized configurations that introduce minimal strain into the lattice. Moreover, previous microscopic model calculations [51] indicate that transitions passing through intermediate AA-like stacking configurations are energetically less favorable. These considerations motivated to use the constraint of $n_i < 2$, since larger displacements are more likely to introduce AA-type stacking regions. With this in mind, we identified three possible geometries for a 3-layer system—taking into account the redundancies caused by symmetry:

$$\vec{n} = [0,\ 0,\ 1], \quad (ABC) \rightarrow (ABA),$$

$$\vec{n} = [0,\ -1,\ -1], \quad (ACB) \rightarrow (ABA),$$

$$\vec{n} = [-1,\ 1,\ 1], \quad (BAC) \rightarrow (ABA).$$

Among these stacking transitions, the configuration with $\vec{n} = [0, 0, 1]$ introduces the least strain into the system, making it the most mechanically favorable. Therefore, we focus our analysis on this configuration in the present study, as it captures the essential physics of the ABA–ABC transition while allowing for a clear and controlled examination of the domain wall structure. A systematic comparison with alternative displacement vectors such as $\vec{n} = [0, -1, -1]$ remains an interesting direction for future work.

The resulting atomic geometry following the applied $\vec{n} = [0, 0, 1]$ displacements is shown in Fig. 1a, which presents close-up snapshots at various locations along the GB, illustrating the gradual structural transition from ABC to ABA stacking. The applied displacement leads to bond stretching across the boundary, where a total shift of one carbon–carbon bond length is accommodated over an effective width of 20 nm. This results in a maximum bond elongation of approximately 1.55%, as visualized in the bond length distribution plotted in Fig. 1b.

Following the construction of the initial flat solitonic geometry, we performed a molecular statics relaxation to obtain the relaxed atomic structure. To relax the geometry, the conjugate gradient method was used in LAMMPS [52]. The Long-range Carbon Bond-Order Potential (LCBOP) [53] accurately described intralayer bonding, while the Dihedral-angle-corrected Registry-dependent Interlayer Potential (DRIP) [54] captured the subtle registry-dependent interlayer interactions crucial for modeling solitons. This combination offers the most recent and physically complete empirical model for multilayer graphene currently available, excluding machine-learning-based potentials (MLIP) that require extensive retraining. During energy minimization, the two ends of the ribbon – comprising pure ABA and ABC stacking regions, each approximately 17 nm wide – were held fixed, while only the intermediate solitonic boundary region, spanning roughly 33 nm, was allowed to relax. This fixing constraint reflects a well-known challenge in modeling: ABC stacking is metastable and easily collapses to ABA in fully relaxed simulations. Several experimental and theoretical works [24,49,55] report similar constraints when stabilizing rhombohedral domains under thermal or mechanical perturbation. By selecting a relaxation region (33 nm) larger than the initial effective soliton width (20 nm), we provided additional space for the induced strain to redistribute more gradually across the structure if needed. The system was relaxed in a fully free-standing configuration to ensure that the intrinsic geometry and strain distribution of the ABC–ABA domain wall develop without artifacts that could otherwise result from constraining fixed layers, when mimicking substrate effects.

Upon relaxation, the stacking domain boundaries developed prominent out-of-plane corrugations, as seen in Fig. 1d, consistent with solitonic deformations previously reported in both scanning probe microscopy studies and atomistic simulations [44,45,56]. The observed corrugations reflect an energetic compromise: the system reduces the unfavorable interlayer potential associated with stacking mismatches by allowing atoms to displace out of plane, while simultaneously alleviating in-plane tensile and shear strains. This results in a solitonic structure where the total energy is minimized through coupled in-plane and out-of-plane distortions. Fig. 1e displays the corrugation profiles of the layers, with the out-of-plane deformation reaching a peak amplitude of 2.2 Å. In addition to the out-of-plane corrugation, significant in-plane atomic redistribution also takes place during relaxation. This is evident in Fig. 1f, where the initial sigmoid displacement profile (colored curve) becomes smoother (black curve), indicating a reduction in the displacement gradient. As a result, the imposed shift is more evenly distributed across the available width of the solitonic region. The relaxed grain boundary exhibits an effective width of 26 nm, corresponding to the region where the majority of the atomic displacement occurs. Bond elongation also drastically reduced after relaxation, from the initial 1.55% to 0.48% residual strain.

This simulation setup is particularly noteworthy for its scalability and precision. Compared to first-principles DFT studies, which are limited in system size, this classical approach allows the modeling of solitons across ribbons exceeding 100 nm in length, making it ideal for resolving large-scale stacking transitions and examining boundary morphology. Moreover, the selection of specific $\vec{n}$-vectors provides a systematic way to tune interlayer registry, and future extensions could quantify their influence on atomic structure.

3. Wave packet dynamical analysis of the transport for the ABC-ABA and ABA-ABC geometries

In WPD modeling the physical system is described by a Hamiltonian and the initial conditions are given by an initial wave function. The method provides the $\psi(\vec{r}; t)$ time-dependent wave function by the solution of the time-dependent Schrödinger equation [34]. We applied the split-operator Fourier transform method, (see SI Section I). By performing a time-energy Fourier transform the $\psi(\vec{r}; E)$ energy-dependent wave function is also available. If the Hamiltonian is written

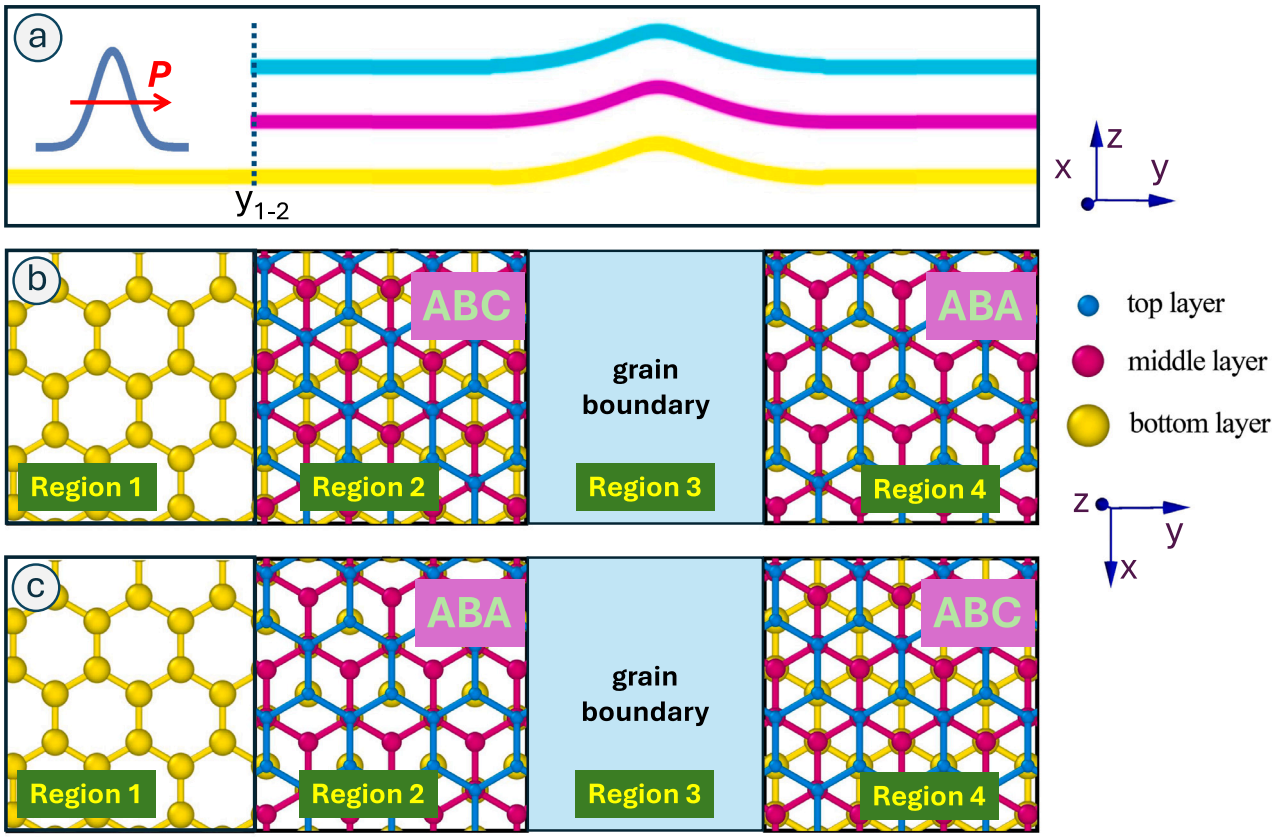

Fig. 2. Model geometry used in the wave packet dynamical calculation, (a) yz cross section, (b), (c) xy cross section. (b) ABC–ABA and (c) ABA–ABC. The wave packet (shown symbolically on the inset of (a)) starts from Region 1, the single layer graphene region. Its initial impulse, P is in the y direction. Region 2 is a perfect ABC (ABA) trilayer, Region 3 (light blue rectangle) is the grain boundary region, Region 4 is a perfect ABA (ABC) trilayer. The spheres representing the atomic positions are drawn progressively thicker in each layer (layer 1: small cyan, layer 2: medium size magenta, layer 3: large yellow), in order to visualize the stacking of the layers. The thickness of the grain boundary and of the width of the initial wave packet is not to scale on the figure. The model geometry and the size of the initial wave packet is infinite (periodic) in the x direction.

in the $\hat{H} = \hat{K} + \hat{V}$ form, where $\hat{K}$ is the free space kinetic energy, then the electronic structure is coded into the potential energy operator $\hat{V}$. To obtain $\hat{V}$ in this work we utilize our recently developed pseudopotential [40], which was constructed for WPD calculations for *van der Waals* stacks of carbon sheets. As we have shown in [40], it correctly describes the electronic structure of AA, AB bilayer graphene, ABC (rhombohedral) trilayer graphene, as well as bulk AA, AB, and ABC graphite, even in case of external electric fields. The functional form of the pseudopotential is a sum of Gaussians centered on the atomic sites and its parameters are given in [40]. These preliminary results demonstrate that a suitable pseudopotential for WPD transport calculations can be reliably constructed using the atomic structure of the modeled ABC–ABA GB.

In order to study the wave packet (WP) reflection from the GB, we constructed a model system specifically for the WPD calculations consisting of four regions: (see Fig. 2) (1) a single-layer graphene (SLG) region acting as a lead, (2) a perfect ABC (or ABA trilayer), (3) the GB region obtained from the molecular statics simulation discussed in previous section, and (4) a perfect ABA (or ABC) trilayer. This geometry models a transport device, where electrons are injected from an electrode into the outer layer of the sample. Comparable configurations can be realized experimentally using top-contacted multilayer graphene devices, where the electrode predominantly couple to the outermost layer. Furthermore a one-to-one experimental geometry could be also achieved by contacting a graphene sheet that protrudes beyond the lower layers, enabling direct injection into a single outer layer. The system is infinite (periodic) in the x direction (parallel to the boundary of the two regions). The WP starts from Region (1), the SLG lead region. As it evolves, a portion is transmitted through the model system, while the remainder is reflected back into Region (1), where we evaluate its reflection probability, denoted by R. The ABA–ABC system was constructed by rotating the fully relaxed ABC–ABA geometry (see Fig. 1) 180° around a vertical axis passing through the center of the GB, effectively swapping the positions of the ABC and ABA regions while preserving the interface structure. Thus we can compare the $R_{ABC-ABA}$ and $R_{ABA-ABC}$ reflection probabilities, whose ratio is characteristic to the rectification properties of this whole transport device geometry. There is a free-space boundary condition at both ends of the model system, representing the source and drain contacts, so that the reflected and transmitted WPs reaching the boundaries are not reflected back into the simulation region.

The initial $\psi(\vec{r};t_0)$ state is constructed [40] from the Bloch states of the SLG numerically calculated from the pseudopotential by a Gaussian convolution centered on a graphene K point along the Γ-M line (see SI Section II).

The initial impulse of the WP is perpendicular to the boundary and its width is infinite in the direction parallel to the boundary (x), i.e. $\vec{p} = p_y\vec{y}$ (see Fig. S1 b). With translational invariance along x, this initial condition is thus best viewed as a planar 'wave front'.

To study the dynamics of the WP, we analyze the four-dimensional wave function dataset $\psi(x,y,z,t)$ by computing integrals of quantum mechanical observables derived from the wave function. As a first step, we calculated two key observables from the wave function: the probability density, $\rho(\vec{r};t) = |\psi(x,y,z;t)|^2$ and the probability current density, $\vec{j}(\vec{r};t)$.

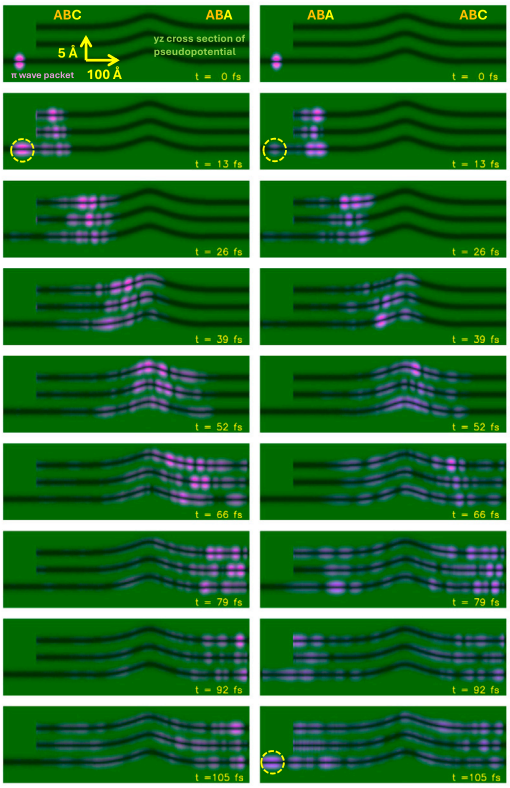

Fig. 3. Wave packet transmission and reflection for the ABC-ABA (left column) and ABA-ABC (right column) grain boundaries. Snapshots of the time dependent probability density of the WP (integrated over x, the coordinate perpendicular to the paper) are shown by the strength of the magenta color. Note the π character of the probability density — it is zero in the graphene sheet and maximum above- and below it. The three dark grey streaks show the graphene layers, their thickness corresponds to the perpendicular size of the π wave function. Note the different horizontal and vertical scale, the z scaling is enlarged by a factor of 48 relative to the y scale. The WP starts from the single layer region on the left. There is a free space boundary condition on the left- and right side. In this figure the reflection events to the single-layer region (at $t = 13$ fs and $t = 105$ fs) are highlighted by yellow dotted circles. See also the video in the Online Supplementary Material.

3.1. Time evolution of the wave packet

To visualize the spatial evolution of the wave packet, we computed two-dimensional projections of the probability density by integrating along the x-direction—perpendicular to the WP momentum within the graphene plane—according to

$$\rho(y,z;t) = \int_{-\infty}^{+\infty} |\psi(x,y,z;t)|^2 \, dx. \tag{3}$$

Snapshots of the resulting $\rho(y,z;t)$ evolution are shown in Fig. 3, illustrating the time-dependent dynamics of the WP in the y–z plane.

At $t = 0$ fs, in both geometries, the initial WP, indicated with magenta color, is localized in Region (1), corresponding to the SLG domain. As the WP enters Region (2) at $t = 4$ fs, it begins to experience the *van der Waals* potential of the second and third graphene layers. This additional perturbation breaks the translational symmetry of the initial single-layer system: the Bloch states of monolayer graphene are no longer eigenstates of the trilayer system. Consequently, the momentum distribution of the WP evolves, and interlayer tunneling gradually develops as a result of the weak interlayer coupling. Upon reaching the single-layer – three-layer boundary some of the WP is reflected back into the SLG region, as seen around $t = 13$ fs. This reflection is much more pronounced for the ABC case, and, as we will see, its energy spectrum is different from that for the ABA case. We will analyze this phenomenon in detail in Section 3.2.

At $t = 30$ fs, the WP reaches the GB and begins a complex scattering process. From this point onward, the two configurations – ABC–ABA and ABA–ABC – exhibit markedly different dynamics. In the ABC–ABA case, the WP transmits through the boundary into the ABA region with minimal reflection, as seen at $t = 66$ fs. In contrast, for the ABA–ABC geometry, a significant portion of the WP is reflected back into the ABA region, with only a small fraction entering the ABC domain. At $t = 92$ fs and $t = 105$ fs (see the lower right panels of Fig. 3), the reflected WP is seen propagating back toward Region (1), the initial single-layer graphene domain (highlighted with a yellow circle).

To assess the overall effect of the device on the WP, we performed a spectral analysis of the backscattered component in the SLG region at a single snapshot, $t = 105$ fs. Even this instantaneous frame already revealed a key feature: a pronounced difference in reflectance between the two geometries within the −0.5 eV to +0.5 eV energy range (see SI Fig. S1), indicating that the distinct band structures of ABA and ABC trilayers play an important role in the reflection process. However, this single snapshot represents only a momentary response of the device, which can fluctuate in time. To obtain the full, time-integrated behavior that would correspond to an experimentally measurable quantity, we evaluated the asymptotic total reflection probability.

To quantitatively determine the transmission and reflection of the WP, we evaluated the y component (that perpendicular to the grain boundary) of the probability current density j_y in the different regions of the device (see Fig. 2a). Integrating over the xz plane gives the net probability current at a given time:

$$I_R(t) = \iint j_y(x,z,y_{1-2};t)\, dx\, dz. \tag{4}$$

The time-dependent reflection is then obtained as the indefinite integral of this current:

$$R(t) = \int_0^t I_R(t')\, dt', \tag{5}$$

where the asymptotic value $R(t \to \infty)$ yields the total reflection probability [57].

We found a total reflection of $R = 0.159$ in the ABA–ABC geometry and only $R = 0.007$ for the ABC–ABA configuration measured in the SLG electrode, indicating more than a twentyfold reduction in backscattering. This highlights a strong anisotropy in the transport behavior across the GB—effectively functioning as a quantum diode.

3.2. Detailed analysis of the factors leading up to the transport asymmetry

To elucidate the origin of the observed transport asymmetry, it is essential to decouple the two primary scattering processes that occur within our device architecture: (i) reflection at the contact between the single-layer graphene (SLG) lead and the perfect ABA/ABC trilayer regions, and (ii) subsequent backscattering from the perfect ABA (ABC) to the perfect ABC (ABA) through a grain boundary.

We found that both scattering processes play an important role in the device response. As we will show in detail, the SLG lead determines the population of the distinct electronic states of the perfect ABA/ABC regions. These electronic states, one linear and one parabolic band in ABA and a cubic band in ABC, have different transmission probabilities during the scattering between the perfect trilayer (ABC and ABA) regions, resulting in a robust directional transport asymmetry (see later Fig. 6). In the subsequent two subsections we analyze the effect of the two interfaces – SLG-ABA(ABC) and ABA(ABC) - ABC(ABA) separately.

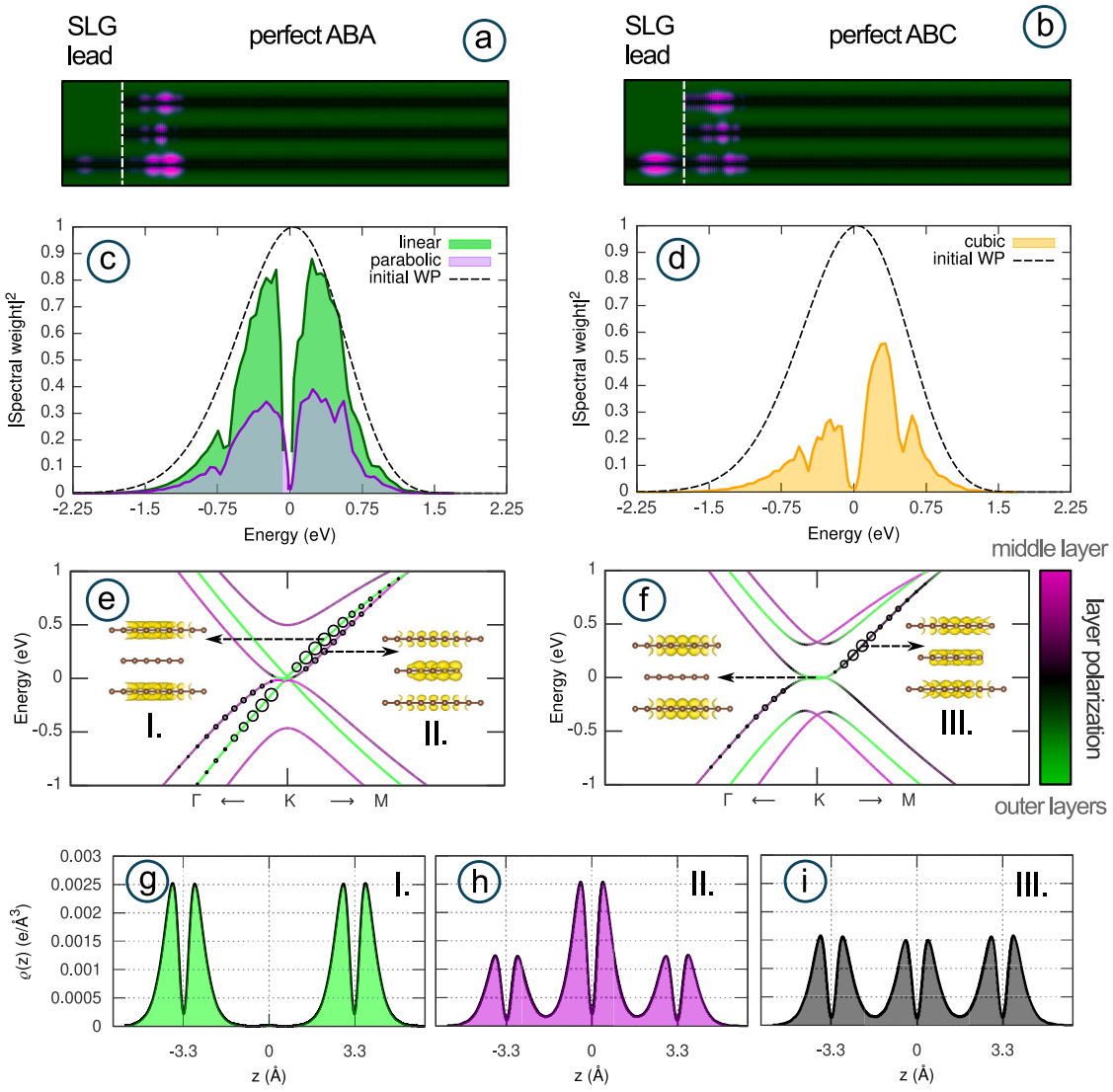

Fig. 4. Wave packet injection from a bottom-contacted single-layer graphene lead into perfect ABA and ABC trilayer graphene domains. a–b, Snapshots of the wave packet (WP) probability density at $t = 13$ fs, showing the injected and reflected portions immediately after interacting with the interface (dashed white line) for the ABA (a) and ABC (b) geometries. **(c–d)** Spectral weight of the injected WP projected onto the bulk trilayer eigenstates for the ABA (c) and ABC (d) domains. The spectrum of the initial WP in the lead is shown as a black dashed line. The height of the functions indicate the spectral weights of the corresponding bands in the transmitted WPs. **(e–f)** DFT-calculated, layer-projected band structures for perfect ABA (e) and ABC (f) trilayer graphene. The color scale indicates layer polarization of the bands, from the middle layer (magenta) to the outer layers (green). The black color indicates the absence of layer polarization, where all three layers contribute equally. Black circles on the bands illustrate, for visual purposes only, the spectral weight of the populated states from the WPD (from c and d), with the radius proportional to the population. Insets show the corresponding real-space DFT charge distributions for representative layer-polarized states. **(g–i)** Planar averaged charge density profiles of the trilayer systems from DFT calculations at specific energies corresponding to the insets (I–III) as a function of the out-of-plane z-direction.

3.2.1. *Effect of the graphene lead*

First, we investigated the influence of the graphene contact. As we saw previously in Fig. 3, the initial contact between the SLG lead and the perfect trilayer region is responsible for a backscattering event. Simultaneously, the transmitted fraction also dictates the population of electronic states within the perfect ABA/ABC regions. In order to separate the effects of the grain boundary from the SLG-ABA(ABC) contact, we built two test geometries containing only the graphene lead and the perfect trilayer region (ABA or ABC) (see Fig. 4a,b). The energy dependent transmission depends on several factors, including matching the group velocities (see SI Section III), the layer polarizations (localization of states on the different layers), and sublattice characters (localization on A/B sites) between the two sides. To quantify the extent to which different states are populated, we calculated the band dependent spectral decomposition of the injected WP to the ABA (ABC) trilayers, by evaluating the $s^b(E;t) = \left|\left\langle \psi(\vec{r};t) \middle| \varphi^b(\vec{r};E) \right\rangle\right|$ scalar products, where the $\varphi^{r,b}(\vec{r};E)$ functions are the Bloch eigenstates in the ABA (ABC) trilayers and b is the band index (see SI Section IV). The spectral weights of the populated states from the graphene lead together with the layer polarization is visualized in the ABA and ABC bandstructures in Fig. 4.

Our analysis reveals that the SLG lead populates the available trilayer modes differently. In the case of the SLG-ABA junction, the lead efficiently populates the monolayer-like (linear) bands of the ABA buffer due to excellent matching in both group velocity and layer character. These linear bands are perfectly localized on the outer layers, as shown by the green lines of the layer projected bandstructure in Fig. 4e and by the spatial distribution of a representative state in Fig. 4g. One of these outer layers is in direct contact with the SLG lead. The efficient population can be seen from the high value of the green

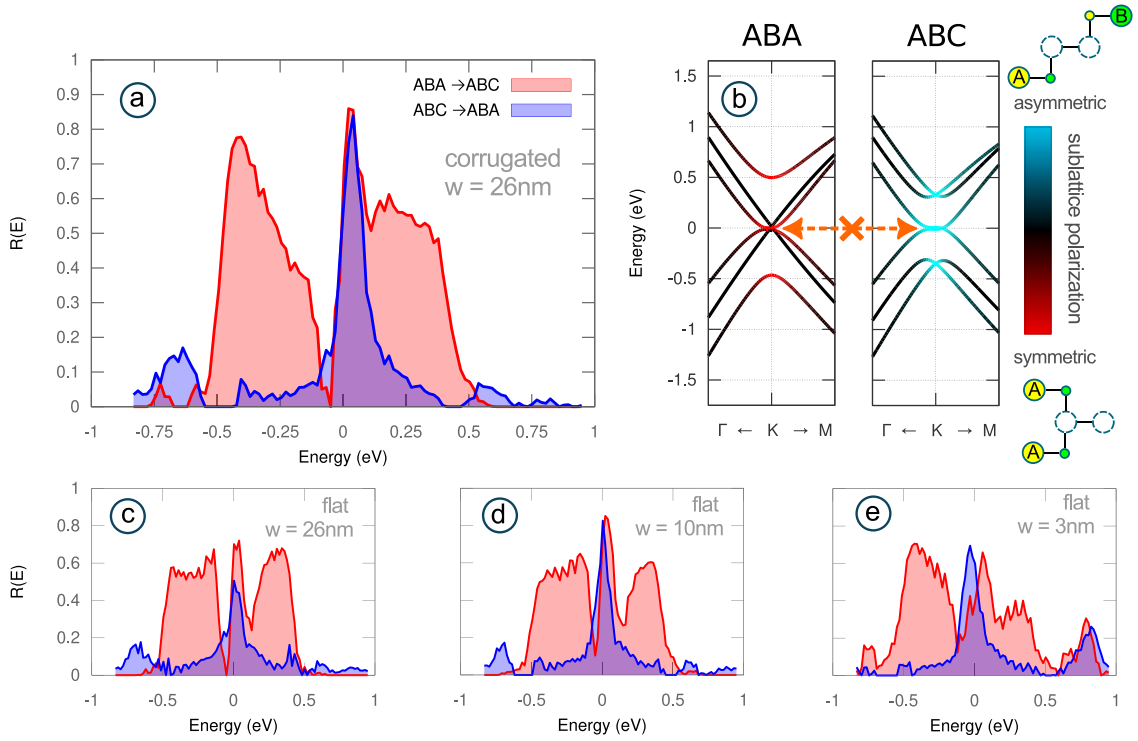

Fig. 5. Direction-dependent reflection of the populated states at an ABA/ABC trilayer graphene grain boundary. (a) Energy-resolved reflection spectrum of the populated states, $R(E)$, for a corrugated grain boundary ($w = 26$ nm). Scattering from ABA→ABC (red area) is compared to ABC→ABA (blue area), revealing a strong, direction-dependent reflection asymmetry (a diode effect). The spectra are normalized to eliminate contact filtering (see SI Section V). Both directions exhibit a prominent reflection peak at the Fermi level ($E = 0$), which is driven by the sublattice symmetry mismatch detailed in figure (b). **(b)** DFT-calculated, sublattice-polarized band structures projected onto the outer layers. The color scale indicates the polarization symmetry between the top and bottom layers: symmetric, when both layers have the same sublattice character (red) or asymmetric with opposing sublattice characters (cyan). Black denotes unpolarized states. The mismatch in this pseudospin texture between the low-energy bands of the two domains (indicated by the orange arrow) is responsible for the reflection peaks at the Fermi level. **(c–e)** Reflection spectra for unrelaxed (flat) grain boundaries of varying widths: $w = 26$ nm (c), $w = 10$ nm (d), and $w = 3$ nm (e).

spectral weights in Fig. 4a. By contrast, AB bilayer-like (parabolic) bands are only weakly excited (see purple spectral curves in Fig. 4c) due to two factors: their lower group velocities near the Fermi level (E_f) compared to the constant Fermi velocity in graphene, and the mismatch in layer character, whereby the parabolic band is localized across all three layers, with the middle layer showing the strongest dominance. This type of layer polarization is indicated by purple lines of the bandstructure in Fig. 4e. A corresponding spatial charge distribution of such a state is visualized in Fig. 4h.

For the SLG–ABC junction, the low-energy states are also localized on the top and bottom layers, as indicated by the green bands near the Fermi level in Fig. 4f. However, their dispersion is much flatter near E_f, which produces a pronounced group-velocity mismatch (see Fig. S2). Injection from the SLG lead is therefore less efficient at low energies, as evidenced by the dip in spectral weight around the Fermi energy (Fig. 4d). The contact thus couples more effectively to channels with higher group velocity. However, at higher energies, these available states are still populated less efficiently than in the ABA case, owing to their distinct, nearly uniform distribution across all three layers, as shown by the black color of the bands in Fig. 4f and by the spatial charge density of a representative state in Fig. 4i. As Fig. 4i demonstrates, the charge concentration on the bottom (contacted) layer is noticeably lower than in Fig. 4g, revealing that fewer states are available for injection thus leading to the reduced spectral weight observed.

Overall, we found that the ABC trilayer was populated less by the SLG lead than the ABA trilayer. We note that the initial state arriving at the grain boundary is not a mixture of all available channels but rather a biased superposition. These distinct population biases established at the contact set the initial conditions for scattering at the grain boundary and play a part in the emergent transport asymmetry.

3.2.2. Grain boundary effects on the populated states

Next, we focus on the scattering process stemming from the perfect ABA (ABC) to the perfect ABC (ABA) through the grain boundary. The total current flowing through this boundary is influenced by both the single layer–trilayer interfaces and trilayer–trilayer interfaces. Here, however, we focus exclusively on the contribution of the latter, i.e. the grain boundary itself. To this end, we compared the currents flowing through the whole device (e.g. SLG-ABA-ABC) to the currents of the test systems introduced in the previous subsection (SLG-ABA). We calculated the energy-dependent reflection amplitude

$$R(E) = 1 - I_{\mathrm{out}}(E)/I_{\mathrm{in}}(E)$$

where $I_{\mathrm{in}}(E)$ is the total incident current summed over all populated modes of the pristine (GB-free) trilayer region, and $I_{\mathrm{out}}(E)$ is the outgoing current of the full device (see details in SI Section V). This ratio effectively normalizes the current, canceling out any transmission components that are invariant to the grain boundary's presence. Therefore, by dividing these currents ($T = I_{out}(E)/I_{in}(E)$), we get exclusively the scattering effect of the grain boundary on the populated states.

Regarding our relaxed GB geometry for both transport directions (ABA→ABC and ABC→ABA), the spectra in Fig. 5a show high reflectivity in a ±50 meV window around the Fermi level. The pronounced asymmetry emerges at higher energies (up to ±0.5 eV), with the ABA→ABC direction exhibiting significantly higher reflection, which is responsible for the diode-like behavior.

We will now examine these energy regions separately. To understand the features observed in the $R(E)$ spectrum, we analyze the scattering process using the bulk band structures of the SLG, ABA, and ABC regions, considering the previously mentioned group velocity

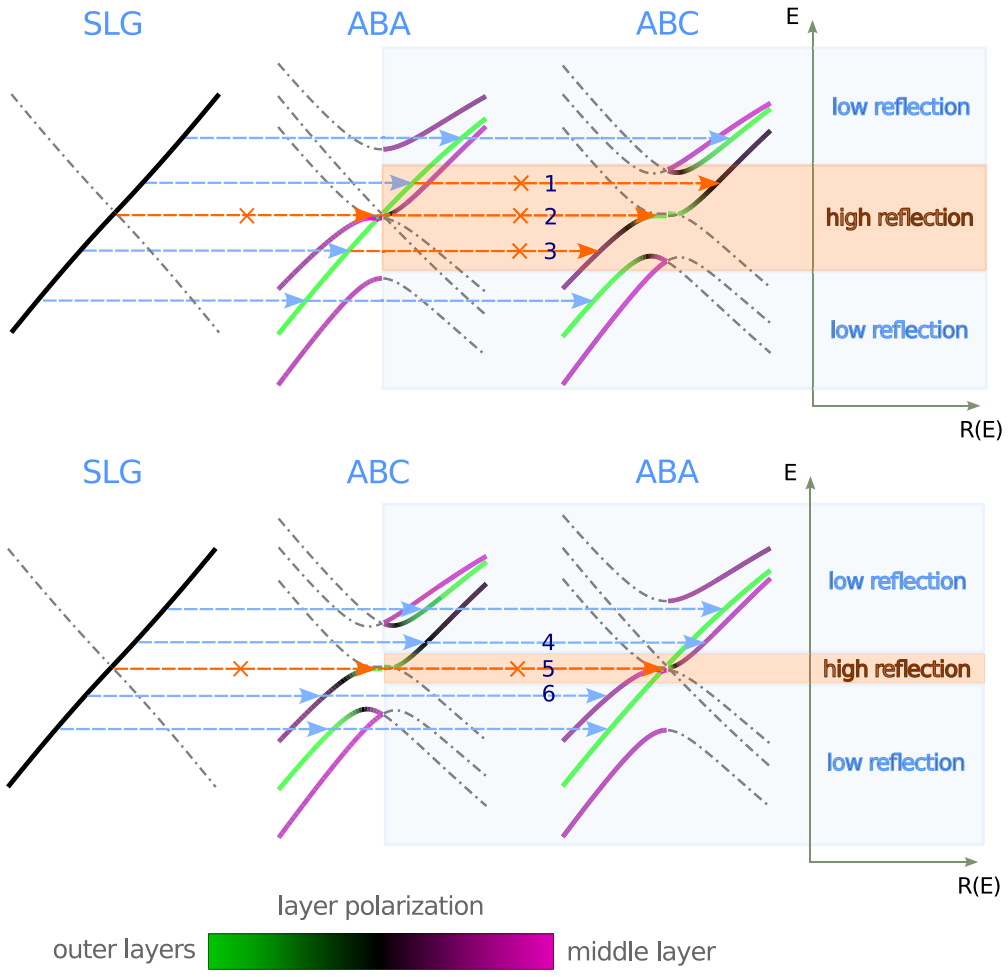

Fig. 6. Schematic interpretation of reflection asymmetry. The diagram illustrates the dominant scattering channels at the ABA/ABC interface using the bulk band structures. Bands are colored according to their layer polarization (green: outer layers; magenta: middle layer, black: equally localized across all layers) shown only for bands with positive group velocity, thus contributing to transport. Dashed arrows indicate scattering paths (numbered in the figure), with light blue representing high-transmission processes and orange indicating strong reflection. **Top Row (SLG → ABA → ABC)**: Injection from the SLG lead primarily populates the linear bands (green) in the ABA domain. Across the grain boundary, these states experience a mismatch with their ABC-domain counterparts in both group velocity and layer polarization, corresponding to green → black **(no. 1)** and green → dark purple **(no. 3)** transitions at the electron and hole sides, respectively. These mismatches lead to high reflections (orange arrows) at the ±0.5 eV domain. **Bottom Row (SLG → ABC → ABA)**: States populating the layer-delocalized cubic bands (black and dark purple) of the ABC domain find well-matched channels in the parabolic bands of the ABA domain, corresponding to black → purple **(no. 4)** and dark-purple → purple **(no. 6)** transitions on the electron and hole sides, respectively. These correspondences facilitate high transmission (blue arrows) within the ±0.5 eV range, except at the Fermi level **(no. 2 and 5)**.

matching, layer polarization, and sublattice polarization. In Fig. 6 we plot the three bandstructure and show also the layer polarization for the ABA and ABC bulk geometries by using the same color scale as in Fig. 4.

(i) Reflection near the Fermi energy. At the Fermi-energy both directions ABA→ABC and ABC→ABA show high reflection (i.e. low transmission) marked by red arrows no. 2 and no. 5 in Fig. 6. Symmetry considerations explain this high reflectivity near E_f as shown in the sublattice-polarized band structures (Fig. 5b). ABA-stacked graphene possesses mirror symmetry but lacks inversion symmetry, whereas ABC-stacked graphene has inversion symmetry but lacks mirror symmetry. The low-energy electronic states, which are localized on the outer layers (see Fig. 4), must conform to these symmetries. In the ABA system, the sublattice polarization of the top and bottom layers must be identical, while in the ABC system they must be opposite. Our DFT calculations confirmed this symmetry effect demonstrating the different sublattice polarization near the Fermi-level (marked by red and blue in Fig. 5b). Consequently, scattering between these low-energy polarized states across the grain boundary is symmetry-forbidden, resulting in high reflection for both transport directions near E_f.

(ii) Reflection below ±0.5 eV**.** Regarding the asymmetry within the ±0.5 eV energy window (see Fig. 5a) the different bands of ABA and ABC explains the effect. For the ABA→ ABC direction, the efficiently populated linear bands in the ABA do not transmit well into the cubic bands of the ABC region due to the different layer polarization character. The linear band localized perfectly in the outer layer (shown by green in Fig. 6) in contrast to the cubic band that is localized across all three layers (shown by black and dark purple in Fig. 6). This results in a broad energy range of high reflectivity (see arrows no. 1 and 3 in Fig. 6). Conversely, for the ABC→ ABA direction, the incoming channels in the ABC cubic band can couple effectively to the parabolic bands of the ABA at range ±0.5 eV, because their layer characters are similar to each other, such that are localized across all three layers (colored with black, dark-purple, or purple in Fig. 6 for processes no 4 and 6.). Their group velocities are also well-matched, opening efficient transmission channels and confining high

reflectivity to a narrow window around E_f. Overall, the pronounced transmission asymmetry observed throughout the ±0.5 eV window in our $R(E)$ function is a direct consequence of the mismatch in the layer localization of differently populated bands of the ABA and ABC trilayers. In ABA stacking, mirror symmetry gives rise to states that are fully localized on the outer layers with vanishing weight on the middle layer (as in Fig. 4 g), whereas in ABC stacking the states are distributed across all three layers (as in Fig. 4 i). As a result, transmission between these two- and three-layer–polarized states is strongly hindered.

(iii) Reflection above ±0.5 eV**.** The reflection decreases above ±0.5 eV that is apparent from the reflection curves in Fig. 5a. These effects are caused by the low- and high-energy parabolic bands of trilayer graphene entering the energy window. This provides additional scattering channels with matched group velocities and layer polarization.

3.3. Effect of the specific structure of the grain boundary

We note that features in the $R(E)$ spectra not captured by this simple band-matching model represent intrinsic properties of the grain boundary, suggesting it can mediate scattering between otherwise decoupled states. One such signature is the prominent dip in reflectivity just below E_f (see Fig. 5a). To test the robustness of our findings, we also performed simulations for various unrelaxed, flat grain boundary model geometries having different GB widths (3 nm, 10 nm, 26 nm). Using these simplified models, we investigate two distinct geometric factors: first, the effect of corrugation, by comparing the relaxed corrugated 26 nm GB to its unrelaxed flat counterpart; and second, the influence of boundary sharpness, by contrasting flat GB geometries with varying widths of 26 nm, 10 nm, and 3 nm. These geometric effects are physically relevant, as features like sharp grain boundaries and strong corrugation are known to facilitate scattering involving large momentum transfers (Δk), which can enable further scattering processes, even intervalley transitions in extreme cases. We found that the key qualitative features – high reflectivity at E_f, a dip below E_f, and significant asymmetry at higher energies – are present in all cases (Fig. 5 c,d,e). However, the details of the precise energy dependence of the reflection function $R(E)$ strongly depend on the particular GB geometry. Regarding corrugation, the relaxed geometry introduces a high reflection peak on the hole side around −0.5 eV (Fig. 5 a), while its flat 26 nm counterpart shows nearly constant reflection (Fig. 5 c). In terms of width, the flat 26 nm GB constant behavior persists for the 10 nm GB. In sharp contrast, the 3 nm GB geometry not only introduces new reflective peaks around +0.75 eV but also causes the reflections at the Fermi level to split in energy for the two different transport directions (see Fig. 5 e). These findings highlight the role of atomic-scale structural details in the precise device performance.

4. Conclusion

We investigated quantum transport across a realistic ABC–ABA stacking boundary in trilayer graphene using large-scale wave packet dynamics simulations and atomic geometries relaxed via molecular statics. The carefully constructed GB faithfully captures key experimental features, including soliton width (~ 20–30 nm), out-of-plane corrugation (~2.2 Å), and a mixed tensile–shear soliton character frequently observed in experimental samples. To probe how such realistic stacking boundaries affect charge transport in an actual device setting, we embedded the relaxed structure into a model transport geometry. In this configuration the electrons are injected into the system through a contact to one of the outer layers of the trilayer graphene. To this end we applied a model, where the wave packet is injected into the trilayer region from a single layer graphene region seamlessly connected to the lower layer of the trilayer graphene. In this geometry our WPD simulations reveal a striking directional asymmetry in transport: wave packets incident from the ABC side transmit almost entirely, while those from the ABA side are mostly reflected.

According to our analysis of the microscopic origins of the anisotropic behavior, the main factors are the different electronic structures of the ABA and ABC graphenes. This is manifested in the different number-, effective mass-, layer- and sublattice polarization of the electronic bands of both of these graphenes. The contact (the SLG lead in our device model) causes a pre-selection process to occur: the bands are differently occupied in the ABA–ABC and ABC–ABA devices, which have different transmission probabilities during the scattering between the ABC and ABA regions, resulting in a robust directional transport asymmetry. The asymmetry is a robust phenomenon: it is present in each of our grain boundary models studied in this paper, while the fine details of the $R(E)$ energy-dependent transmission functions vary with the specific geometry. Further work is necessary to clarify the details of this connection.

The distinct stacking symmetries of ABA and ABC graphene result in different phonon spectra, as has been shown in both calculations [58] and experiments [59]. Thus, ABA–ABC grain boundaries can exhibit significant interfacial heat resistance and even thermal rectification, which can enable thermal management and thermal-logic [60] functionalities.

To experimentally study this newly discovered anisotropy of the ABA-ABC transport, we envisage a Scanning Tunneling Microscopy (STM) or spectroscopy (STS) experiment, where the electrons are injected also into the upper layer of the trilayer graphene by the STM tip — similar to our model, where the wave packet arrives at one of the outer layers. In future studies, our pseudopotential-based wave packet approach offers a powerful framework for exploring electrostatic gating effects, enabling tunable and gate-controllable rectification in multilayer graphene architectures, paving the way for future advancements in graphene-based electronics.

CRediT authorship contribution statement

Géza I. Márk: Writing – review & editing, Writing – original draft, Visualization, Supervision, Software, Methodology, Conceptualization. **Márton Szendrő:** Writing – review & editing, Software, Methodology, Investigation, Conceptualization. **Alexandre Mayer:** Writing – review & editing. **Zoltán Simon:** Software. **Péter Vancsó:** Writing – review & editing, Investigation,Conceptualization.

Declaration of competing interest

The authors declare that they have no known competing financial interests or personal relationships that could have appeared to influence the work reported in this paper.

The author is an Editorial Board Member/Editor-in-Chief/Associate Editor/Guest Editor for this journal and was not involved in the editorial review or the decision to publish this article.

Acknowledgments

The work has been supported by the Belgian FNRS. P.V. acknowledges support from the National Research, Development and Innovation Office (NKFIH) in Hungary, through Grant No. FK-142985. M.SZ. acknowledges the Digital Government Development and Project Management Ltd. for awarding access to the Komondor HPC facility based in Hungary and the support from the Bolyai János fellowship of the Hungarian Academy of Sciences. A.M. is funded by the Fund for Scientific Research (F.R.S.-FNRS) of Belgium. Helpful discussions with Ph. Lambin and P. Nemes-Incze are gratefully acknowledged.

Appendix A. Supplementary data

Supplementary material related to this article can be found online at https://doi.org/10.1016/j.cartre.2025.100589.

Data availability

Data will be made available on request.

References

[1] W. Yao, B. Wu, Y. Liu, Growth and grain boundaries in 2D materials, ACS Nano 14 (8) (2020) 9320–9346.

[2] S.-J. Yang, M.-Y. Choi, C.-J. Kim, Engineering grain boundaries in two-dimensional electronic materials, Adv. Mater. 35 (4) (2023) 2203425.

[3] A.K. Majee, C.J. Foss, Z. Aksamija, Impact of mismatch angle on electronic transport across grain boundaries and interfaces in 2D materials, Sci. Rep. 7 (1) (2017) 16597.

[4] V.H. Nguyen, T.X. Hoang, P. Dollfus, J.-C. Charlier, Transport properties through graphene grain boundaries: Strain effects versus lattice symmetry, Nanoscale 8 (22) (2016) 11658–11673.

[5] Q. Yu, L.A. Jauregui, W. Wu, R. Colby, J. Tian, Z. Su, H. Cao, Z. Liu, D. Pandey, D. Wei, T.F. Chung, P. Peng, N.P. Guisinger, E.A. Stach, J. Bao, S.-S. Pei, Y.P. Chen, Control and characterization of individual grains and grain boundaries in graphene grown by chemical vapour deposition, Nat. Mater. 10 (6) (2011) 443–449.

[6] A.W. Tsen, L. Brown, M.P. Levendorf, F. Ghahari, P.Y. Huang, R.W. Havener, C.S. Ruiz-Vargas, D.A. Muller, P. Kim, J. Park, Tailoring electrical transport across grain boundaries in polycrystalline graphene, Science 336 (6085) (2012) 1143–1146.

[7] H. Zhang, G. Lee, C. Gong, L. Colombo, K. Cho, Grain boundary effect on electrical transport properties of graphene, J. Phys. Chem. C 118 (5) (2014) 2338–2343.

[8] T. Ma, Z. Liu, J. Wen, Y. Gao, X. Ren, H. Chen, C. Jin, X.-L. Ma, N. Xu, H.-M. Cheng, W. Ren, Tailoring the thermal and electrical transport properties of graphene films by grain size engineering, Nat. Commun. 8 (1) (2017) 14486.

[9] P. Nemes-Incze, P. Vancsó, Z. Osváth, G.I. Márk, X. Jin, Y.-S. Kim, C. Hwang, P. Lambin, C. Chapelier, L. PéterBiró, Electronic states of disordered grain boundaries in graphene prepared by chemical vapor deposition, Carbon 64 (2013) 178–186.

[10] D. Akinwande, C. Huyghebaert, C.-H. Wang, M.I. Serna, S. Goossens, L.-J. Li, H.-S.P. Wong, F.H.L. Koppens, Graphene and two-dimensional materials for silicon technology, Nature 573 (7775) (2019) 507–518.

[11] P.J. Sarsfield, S. Slizovskiy, M. Koshino, V. Fal'ko, Electronic properties of stacking faults in Bernal graphite, Npj Comput. Mater. 11 (1) (2025) 142.

[12] E. Koren, A.W. Knoll, E. Lörtscher, U. Duerig, Direct experimental observation of stacking fault scattering in highly oriented pyrolytic graphite meso-structures, Nat. Commun. 5 (1) (2014) 5837.

[13] F. Zhang, B. Sahu, H. Min, A.H. MacDonald, Band structure of ABC-stacked graphene trilayers, Phys. Rev. B 82 (3) (2010) 035409.

[14] H. Min, A.H. MacDonald, Electronic structure of multilayer graphene, Progr. Theoret. Phys. Suppl. 176 (2008) 227–252.

[15] W.P. Su, J.R. Schrieffer, A.J. Heeger, Solitons in polyacetylene, Phys. Rev. Lett. 42 (25) (1979) 1698–1701.

[16] Y. Shi, S. Xu, Y. Yang, S. Slizovskiy, S.V. Morozov, S.-K. Son, S. Ozdemir, C. Mullan, J. Barrier, J. Yin, A.I. Berdyugin, B.A. Piot, T. Taniguchi, K. Watanabe, V.I. Fal'ko, K.S. Novoselov, A.K. Geim, A. Mishchenko, Electronic phase separation in multilayer rhombohedral graphite, Nature 584 (7820) (2020) 210–214.

[17] H. Zhou, T. Xie, T. Taniguchi, K. Watanabe, A.F. Young, Superconductivity in rhombohedral trilayer graphene, Nature 598 (7881) (2021) 434–438.

[18] Z. Lu, T. Han, Y. Yao, Z. Hadjri, J. Yang, J. Seo, L. Shi, S. Ye, K. Watanabe, T. Taniguchi, L. Ju, Extended quantum anomalous hall states in graphene/hBN moiré superlattices, Nature 637 (8048) (2025) 1090–1095.

[19] A. Kerelsky, C. Rubio-Verdú, L. Xian, D.M. Kennes, D. Halbertal, N. Finney, L. Song, S. Turkel, L. Wang, K. Watanabe, T. Taniguchi, J. Hone, C. Dean, D.N. Basov, A. Rubio, A.N. Pasupathy, Moiréless correlations in ABCA graphene, Proc. Natl. Acad. Sci. 118 (4) (2021) e2017366118.

[20] I. Hagymási, M.S. Mohd Isa, Z. Tajkov, K. Márity, L. Oroszlány, J. Koltai, A. Alassaf, P. Kun, K. Kandrai, A. Pálinkás, P. Vancsó, L. Tapasztó, P. Nemes-Incze, Observation of competing, correlated ground states in the flat band of rhombohedral graphite, Sci. Adv. 8 (35) (2022) eabo6879.

[21] Y. Zhang, Y.-Y. Zhou, S. Zhang, H. Cai, L.-H. Tong, W.-Y. Liao, R.-J. Zou, S.-M. Xue, Y. Tian, T. Chen, Q. Tian, C. Zhang, Y. Wang, X. Zou, X. Liu, Y. Hu, Y.-N. Ren, L. Zhang, L. Zhang, W.-X. Wang, L. He, L. Liao, Z. Qin, L.-J. Yin, Layer-dependent evolution of electronic structures and correlations in rhombohedral multilayer graphene, Nature Nanotechnology 20 (2) (2025) 222–228.

[22] H.A. Wilhelm, B. Croset, G. Medjahdi, Proportion and dispersion of rhombohedral sequences in the hexagonal structure of graphite powders, Carbon 45 (12) (2007) 2356–2364.

[23] C.H. Lui, Z. Li, Z. Chen, P.V. Klimov, L.E. Brus, T.F. Heinz, Imaging stacking order in few-layer graphene, Nano Lett. 11 (1) (2011) 164–169.

[24] W. Zhang, J. Yan, C.-H. Chen, L. Lei, J.-L. Kuo, Z. Shen, L.-J. Li, Molecular adsorption induces the transformation of rhombohedral- to bernal-stacking order in trilayer graphene, Nat. Commun. 4 (1) (2013) 2074.

[25] L. Jiang, S. Wang, Z. Shi, C. Jin, M.I.B. Utama, S. Zhao, Y.-R. Shen, H.-J. Gao, G. Zhang, F. Wang, Manipulation of domain-wall solitons in bi- and trilayer graphene, Nature Nanotechnology 13 (3) (2018) 204–208.

[26] J. Zhang, J. Han, G. Peng, X. Yang, X. Yuan, Y. Li, J. Chen, W. Xu, K. Liu, Z. Zhu, W. Cao, Z. Han, J. Dai, M. Zhu, S. Qin, K.S. Novoselov, Light-induced irreversible structural phase transition in trilayer graphene, Light.: Sci. Appl. 9 (1) (2020) 174.

[27] S. Zhang, Q. Xu, Y. Hou, A. Song, Y. Ma, L. Gao, M. Zhu, T. Ma, L. Liu, X.-Q. Feng, Q. Li, Domino-like stacking order switching in twisted monolayer–multilayer graphene, Nat. Mater. 21 (6) (2022) 621–626.

[28] D.S. Schneider, L. Lucchesi, E. Reato, Z. Wang, A. Piacentini, J. Bolten, D. Marian, E.G. Marin, A. Radenovic, Z. Wang, G. Fiori, A. Kis, G. Iannaccone, D. Neumaier, M.C. Lemme, CVD graphene contacts for lateral heterostructure MoS2 field effect transistors, Npj 2D Mater. Appl. 8 (1) (2024) 35.

[29] L. Wang, I. Meric, P.Y. Huang, Q. Gao, Y. Gao, H. Tran, T. Taniguchi, K. Watanabe, L.M. Campos, D.A. Muller, J. Guo, P. Kim, J. Hone, K.L. Shepard, C.R. Dean, One-dimensional electrical contact to a two-dimensional material, Science 342 (6158) (2013) 614–617.

[30] A. El Mouhafid, M. Hassane Saley, A. Jellal, Transport properties in ABC-aba-ABC trilayer graphene junctions, Phys. Scr. 99 (7) (2024) 075910, http://dx.doi.org/10.1088/1402-4896/ad5058.

[31] M. Grandadam, S. Pinon, C. Bena, C. Pepin, Interface states at the boundary between ABC and ABA multilayer graphene structures, 2021, arXiv:2106.15627.

[32] M. Yankowitz, J.I.-J. Wang, A.G. Birdwell, Y.-A. Chen, K. Watanabe, T. Taniguchi, P. Jacquod, P. San-Jose, P. Jarillo-Herrero, B.J. LeRoy, Electric field control of soliton motion and stacking in trilayer graphene, Nat. Mater. 13 (8) (2014) 786–789.

[33] A. Dey, A. Azizimanesh, S.M. Wu, H. Askari, Uniaxial strain-induced stacking order change in trilayer graphene, ACS Appl. Mater. & Interfaces 16 (6) (2024) 8169–8183.

[34] B.M. Garraway, K.-A. Suominen, Wave-packet dynamics: New physics and chemistry in femto-time, Rep. Progr. Phys. 58 (4) (1995) 365, http://dx.doi.org/10.1088/0034-4885/58/4/001.

[35] I.R. Lavor, D.R. da Costa, A. Chaves, S.H.R. Sena, G.A. Farias, B. Van Duppen, F.M. Peeters, Effect of zitterbewegung on the propagation of wave packets in ABC-stacked multilayer graphene: An analytical and computational approach, J. Phys.: Condens. Matter. 33 (9) (2020) 095503.

[36] A. Chaves, Energy shift and conduction-to-valence band transition mediated by a time-dependent potential barrier in graphene, Phys. Rev. B 92 (12) (2015).

[37] H.M. Abdullah, D.R. Da Costa, H. Bahlouli, A. Chaves, F.M. Peeters, B. Van Duppen, Electron collimation at van Der Waals domain walls in bilayer graphene, Phys. Rev. B 100 (4) (2019) 045137.

[38] L.S. Cavalcante, All-strain based valley filter in graphene nanoribbons using snake states, Phys. Rev. B 94 (7) (2016).

[39] D.R. da Costa, Valley filtering using electrostatic potentials in bilayer graphene, Phys. Rev. B 92 (4) (2015).

[40] G.I. Márk, P. Vancsó, A. Mayer, New local pseudopotential for multilayer carbon materials and its application in wave packet dynamics, Carbon Trends 13 (2023) 100310.

[41] P. Vancsó, G.I. Márk, P. Lambin, A. Mayer, Y.-S. Kim, C. Hwang, L.P. Biró, Electronic transport through ordered and disordered graphene grain boundaries, Carbon 64 (2013) 101–110.

[42] P. Vancsó, G.I. Márk, P. Lambin, A. Mayer, C. Hwang, L.P. Biró, Effect of the disorder in graphene grain boundaries: A wave packet dynamics study, Appl. Surf. Sci. 291 (2014) 58–63.

[43] H. Wu, X. Yu, M. Zhu, Z. Zhu, J. Zhang, S. Zhang, S. Qin, G. Wang, G. Peng, J. Dai, K.S. Novoselov, Direct visualization and manipulation of stacking orders in few-layer graphene by dynamic atomic force microscopy, J. Phys. Chem. Lett. 12 (30) (2021) 7328–7334.

[44] S.-Y. Li, H. Jiang, J.-J. Zhou, H. Liu, F. Zhang, L. He, Corrugation induced stacking solitons with topologically confined states in gapped bilayer graphene, 2016, arXiv:1609.03313.

[45] J.S. Alden, A.W. Tsen, P.Y. Huang, R. Hovden, L. Brown, J. Park, D.A. Muller, P.L. McEuen, Strain solitons and topological defects in bilayer graphene, Proc. Natl. Acad. Sci. 110 (28) (2013) 11256–11260.

[46] L.-J. Yin, W.-X. Wang, Y. Zhang, Y.-Y. Ou, H.-T. Zhang, C.-Y. Shen, L. He, Observation of chirality transition of quasiparticles at stacking solitons in trilayer graphene, Phys. Rev. B 95 (8) (2017) 081402.

[47] B.-Y. Jiang, G.-X. Ni, Z. Addison, J.K. Shi, X. Liu, S.Y.F. Zhao, P. Kim, E.J. Mele, D.N. Basov, M.M. Fogler, Plasmon reflections by topological electronic boundaries in bilayer graphene, Nano Lett. 17 (11) (2017) 7080–7085.

[48] P. Shen, X. Zhou, J. Chen, A. Deng, B. Lyu, Z. Zhang, S. Lou, S. Ma, B. Wei, Z. Shi, Quick identification of ABC trilayer graphene at nanoscale resolution via a near-field optical route, Mater. Futur. 2 (1) (2023) 015301, http://dx.doi.org/10.1088/2752-5724/acbecd.

[49] F.R. Geisenhof, F. Winterer, S. Wakolbinger, T.D. Gokus, Y.C. Durmaz, D. Priesack, J. Lenz, F. Keilmann, K. Watanabe, T. Taniguchi, R. Guerrero-Avilés, M. Pelc, A. Ayuela, R.T. Weitz, Anisotropic strain-induced soliton movement changes stacking order and band structure of graphene multilayers: Implications for charge transport, ACS Appl. Nano Mater. 2 (9) (2019) 6067–6075.

[50] X. Zan, X. Guo, A. Deng, Z. Huang, L. Liu, F. Wu, Y. Yuan, J. Zhao, Y. Peng, L. Li, Y. Zhang, X. Li, J. Zhu, J. Dong, D. Shi, W. Yang, X. Yang, Z. Shi, L. Du, Q. Dai, G. Zhang, Electron/infrared-phonon coupling in ABC trilayer graphene, Nat. Commun. 15 (1) (2024) 1888.

[51] J.P. Nery, M. Calandra, F. Mauri, Long-range rhombohedral-stacked graphene through shear, Nano Lett. 20 (7) (2020) 5017–5023.

[52] A.P. Thompson, H.M. Aktulga, R. Berger, D.S. Bolintineanu, W.M. Brown, P.S. Crozier, P.J. In 'T Veld, A. Kohlmeyer, S.G. Moore, T.D. Nguyen, R. Shan, M.J. Stevens, J. Tranchida, C. Trott, S.J. Plimpton, LAMMPS - a flexible simulation tool for particle-based materials modeling at the atomic, meso, and continuum scales, Comput. Phys. Comm. 271 (2022) 108171.

[53] J.H. Los, A. Fasolino, Intrinsic long-range bond-order potential for carbon: Performance in Monte Carlo simulations of graphitization, Phys. Rev. B 68 (2) (2003) 024107.

[54] M. Wen, S. Carr, S. Fang, E. Kaxiras, E.B. Tadmor, Dihedral-angle-corrected registry-dependent interlayer potential for multilayer graphene structures, Phys. Rev. B 98 (23) (2018) 235404.

[55] T. Latychevskaia, S.-K. Son, Y. Yang, D. Chancellor, M. Brown, S. Ozdemir, I. Madan, G. Berruto, F. Carbone, A. Mishchenko, K.S. Novoselov, Stacking transition in rhombohedral graphite, Front. Phys. 14 (1) (2018) 13608.

[56] J. Lin, W. Fang, W. Zhou, A.R. Lupini, J.C. Idrobo, J. Kong, S.J. Pennycook, S.T. Pantelides, AC/AB Stacking Boundaries in bilayer graphene, Nano Lett. 13 (7) (2013) 3262–3268.

[57] G.I. Márk, L.P. Biró, P. Lambin, Calculation of axial charge spreading in carbon nanotubes and nanotube y junctions during STM measurement, Phys. Rev. B 70 (11) (2004) 115423.

[58] J.-A. Yan, W.Y. Ruan, M.Y. Chou, Phonon dispersions and vibrational properties of monolayer, bilayer, and trilayer graphene: Density-functional perturbation theory, Phys. Rev. B 77 (2008) 125401.

[59] C. Cong, T. Yu, K. Sato, J. Shang, R. Saito, G.F. Dresselhaus, M.S. Dresselhaus, Raman characterization of ABA- and ABC-stacked trilayer graphene, ACS Nano 5 (11) (2011) 8760–8768, http://dx.doi.org/10.1021/nn203472f, PMID: 21962035.

[60] N. Li, J. Ren, L. Wang, G. Zhang, P. Hänggi, B. Li, Colloquium: Phononics: Manipulating heat flow with electronic analogs and beyond, Rev. Modern Phys. 84 (2012) 1045–1066.